

ARTICLE

Received 24 Aug 2014 | Accepted 5 Mar 2015 | Published 21 Apr 2015

DOI: 10.1038/ncomms7849

Inhomogeneity of the ultrafast insulator-to-metal transition dynamics of VO₂

Brian T. O'Callahan¹, Andrew C. Jones¹, Jae Hyung Park², David H. Cobden², Joanna M. Atkin^{1,3}
& Markus B. Raschke¹

The insulator-metal transition (IMT) of vanadium dioxide (VO₂) has remained a long-standing challenge in correlated electron physics since its discovery five decades ago. Most interpretations of experimental observations have implicitly assumed a homogeneous material response. Here we reveal inhomogeneous behaviour of even individual VO₂ microcrystals using pump-probe microscopy and nanoimaging. The timescales of the ultrafast IMT vary from 40 ± 8 fs, that is, shorter than a suggested phonon bottleneck, to 200 ± 20 fs, uncorrelated with crystal size, transition temperature and initial insulating structural phase, with average value similar to results from polycrystalline thin-film studies. In combination with the observed sensitive variations in the thermal nanodomain IMT behaviour, this suggests that the IMT is highly susceptible to local changes in, for example, doping, defects and strain. Our results suggest an electronic mechanism dominating the photoinduced IMT, but also highlight the difficulty to deduce microscopic mechanisms when the true intrinsic material response is yet unclear.

¹Department of Physics, Department of Chemistry, and JILA, University of Colorado, Boulder, Colorado, 80309, USA. ²Department of Physics, University of Washington, Seattle, Washington 98195, USA. ³Department of Chemistry, University of North Carolina, Chapel Hill, North Carolina 27599, USA. Correspondence and requests for materials should be addressed to J.M.A. (email: jatkin@live.unc.edu) or to M.B.R. (email: markus.raschke@colorado.edu).

Vanadium dioxide (VO_2) is one of the prototypical correlated-electron materials, exhibiting an insulator-metal transition (IMT), with a change in resistivity of several orders of magnitude that can be induced thermally at $T \sim 340$ K (refs 1,2), or optically³. The photoinduced IMT occurs on subpicosecond timescales, and therefore has a non-thermal basis. This ultrafast transition has been studied using a wide variety of spectroscopies, with short-pulse optical^{3–6}, terahertz^{7–9}, X-ray^{10–12} and electron diffraction^{13–15} techniques. These studies have addressed the ultrafast electron dynamics and lattice structural processes that occur during the transition, in addition to slower behaviour over multi-picosecond to nanosecond timescales. However, the mechanism underlying both the thermal and photoinduced IMT remains unclear. While insulating VO_2 is clearly not a band insulator¹⁶, the importance of electron correlations and electron-phonon coupling for its properties remain unclear after more than half a century of study, and experimental results conflict with both Mott or Peierls explanations^{7,16–19}. For example, degenerate pump-probe studies⁵ revealed a limiting transition timescale of 75 fs, suggesting a phonon bottleneck and therefore a structurally limited transition. In contrast, the observation of coherent phonon oscillations above the apparent threshold for triggering the photoinduced phase transition⁷ indicates that the photoinduced IMT is decoupled from the structural transition.

Much of the work on VO_2 has focused on polycrystalline thin films, grown by a variety of techniques²⁰. Recently, differences observed in the ultrafast and thermal properties due to anisotropy and grain size in polycrystalline and epitaxial thin film samples^{9,21–23} suggest that growth conditions can substantially modify the measured response. These results contributed to the confusion in the interpretation of previous measurements. Furthermore, most spectroscopy techniques average over multiple crystallites, subject to large inhomogeneous strain, which could, for example, create mixtures of different competing phases. While nanoimaging techniques such as scattering scanning near-field optical microscopy (*s*-SNOM)¹⁸ can access the heterogeneity in thin films, the complicating extrinsic interactions among crystallites make results difficult to interpret.

To overcome the limitations of averaging over ensembles of crystallites and other heterogeneities, we investigate individual

VO_2 single microcrystals. We perform degenerate pump-probe microscopy to monitor the femtosecond dynamics following the ultrafast photoexcitation. In addition, we use infrared *s*-SNOM to probe the nanoscopic details of the evolution of the spatial phase competition in the thermal IMT. These studies allow us to observe the inhomogeneity in the dynamics among the microcrystals measured, finding highly variable timescales associated with the photoinduced bandgap reorganization. In combination with micro-Raman spectroscopy, we systematically study the relationship of crystallographic orientation, insulating phase and temperature to the photoinduced response dynamics. With *s*-SNOM infrared nanoimaging, we monitor the growth and evolution of metallic and insulating domains through the thermal transition with 10-nm spatial resolution, and find highly temperature sensitive variations in the spatial organization of the domain structure in the individual single crystals. These results suggest a unusually high sensitivity of both the photoinduced and thermal IMT of VO_2 to yet unresolved small perturbations in the form of defects or strain.

Results

Single-crystal pump-probe microscopy. A schematic of the degenerate pump-probe experiment is shown in Fig. 1a, with details described in the Methods section. We perform frequency-resolved optical gating (FROG) of the laser pulses (Fig. 1b) and determine a pulse duration of ~ 45 fs. We use the pulse characteristics (Fig. 1c) as parameters for the fit of the transient reflectivity (see Results section), to resolve 10 s of fs dynamics of the photoinduced transition by deconvolution.

The VO_2 microcrystals that we study are grown by vapour transport²⁴. They show an abrupt, first-order transition in the absence of strain or doping²⁵, in contrast to the percolation behaviour observed in thin-film samples¹⁸. The crystals vary in size (Fig. 1d), and are highly structurally homogeneous, with a flat surface (root mean squared roughness < 1.8 nm).

We characterize the crystallographic orientation, insulating phase and thermal transition temperature using micro-Raman spectroscopy and *s*-SNOM²⁶ for all of the microcrystals measured in these experiments. In the Raman spectra, the shift of the $\omega_{\text{V-O}}$ Raman mode, at ~ 600 cm^{-1} , allows us to estimate the amount

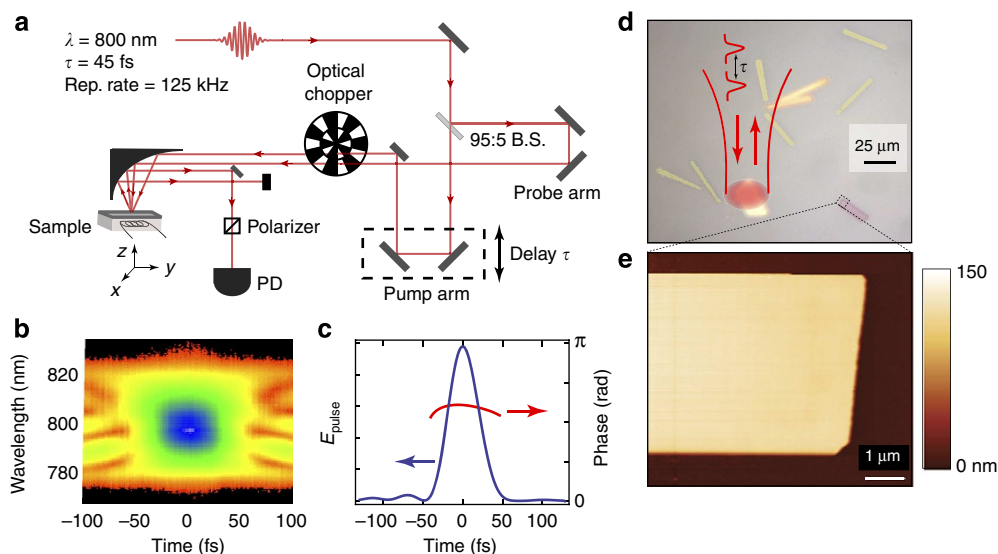


Figure 1 | Single-crystal VO_2 ultrafast pump-probe microscopy (a) Schematic of optical layout. (b) Typical FROG spectrogram of pulse, with (c) full phase and amplitude reconstruction in time domain showing ~ 45 fs pulse duration and small chirp. (d) Optical microscope image of VO_2 microcrystals on Si/ SiO_2 substrate. (e) Atomic force microscopy topography showing the homogeneous nature of the microcrystals.

of strain within the crystal due to substrate interactions or doping. Three possible insulating structures can be distinguished, monoclinic 1 (M1), intermediate triclinic (T) and monoclinic 2 (M2), with increasing degrees of strain²⁷ (Fig. 2a). With their well-defined, controllable strain state and ability to withstand a high degree of strain, microcrystal samples have been studied to investigate the strain-temperature phase diagrams for VO₂ (see Fig. 2b)^{27–31}. The very low-luminescence background and narrow linewidths in Raman spectroscopy indicate a low defect density and confirm a high structural quality of the VO₂ microcrystals.

For low pump fluences, the transient reflectivity response shows an initial electronic excitation, due to the above-gap excitation of the pump, followed by relaxation on a picosecond timescale, as seen in Fig. 2c. Probing at 800 nm (1.55 eV), the response is expected to be dominated by electrons in the d_{||} bands close to the Fermi level^{6,32,33}. The modulations in the reflectivity signal indicate the excitation of coherent phonons in the insulating phase³⁴.

An orientational anisotropy is evident in the relaxation and coherent phonon behaviour, with faster decay and more prominent oscillations for probe polarization perpendicular (pump parallel) to the crystallographic *c_R*-axis (black line), compared with probe parallel (pump perpendicular; red line). The Fourier transform phonon spectrum, shown in Fig. 2d, reveals an even more pronounced anisotropy. For probe polarization perpendicular to the *c_R* axis, only one low energy phonon peak is resolved, at $\sim 200\text{ cm}^{-1}$ (6 THz). For parallel

probe polarization, both phonon modes emerge, with the second at $\sim 225\text{ cm}^{-1}$ (6.7 THz). The reflectivity change at 3 ps also shows an angular anisotropy, with a $\cos^2\theta$ dependence with angle θ of probe polarization with respect to the *c_R* axis (Fig. 2e).

At higher fluences, the coherent phonon response is diminished, eventually vanishing for fluences sufficiently high to drive the microcrystal through the photoinduced IMT (Fig. 3a). The persistence of the reflectivity change (up to microseconds) indicates a metastable metal-like state. However, without a simultaneous structural probe, we cannot determine the crystallographic structure during this period and whether this state corresponds to a rutile or monoclinic metallic state^{19,35,36}. The inset shows the reflectivity $-\Delta R/R$ at 1 ps plotted as a function of fluence, to derive the threshold fluence F_{th} . F_{th} for different microcrystals varies between 2 and 6 mJ cm⁻², which we attribute to variable coupling to the substrate. These values are close to or slightly lower than those observed in thin films, which range from $\sim 5.5\text{ mJ cm}^{-2}$ up to $>15\text{ mJ cm}^{-2}$ (refs 6,11,36,37), due to stronger substrate coupling.

To quantify the transition dynamics and relate to the physical characteristics of the different microcrystals, we fit the above-threshold transient reflectivity behaviour to $-\Delta R/R(t) = I(t) \otimes f(t)$. Here $f(t)$, the response function of the microcrystal, is convolved with $I(t)$, the transient intensity of the pulse from FROG analysis, which accounts for the time resolution and the step-like excitation at $t=0$ without a priori assumptions about pulse duration or shape (see Methods section

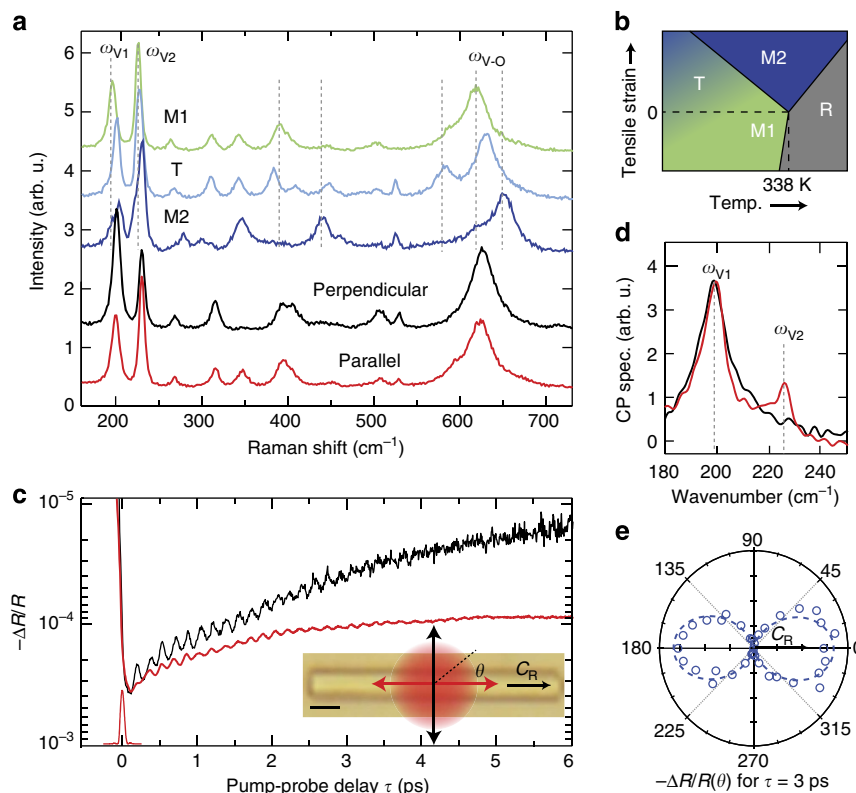


Figure 2 | Insulating microcrystal phase characterization (a) Raman spectra of the three insulating phases, M1 (green, crystal #1), M2 (dark blue, crystal #20) and intermediate triclinic T (light blue, crystal #4). Perpendicular (black) and parallel (red) Raman polarization with respect to *c_R* of a microcrystal in the M1 phase. (b) Strain-temperature phase diagram showing relation of three insulating phases to metallic rutile phase (gray)^{27,28}. (c) Transient reflectivity traces of crystal #29, $-\Delta R/R$, for low fluence with coherent phonon excitation, with probe polarization parallel (red) and perpendicular (black) to the *c_R* axis. The pump pulse is shown in red near time zero. Inset: corresponding image of a microcrystal illustrating the probe polarization geometry. Scale bar, 5 μm . (d) Fourier transform spectra of the reflectivity traces, exhibiting phonon modes at ~ 200 and $\sim 220\text{ cm}^{-1}$. (e) Reflectivity at 3 ps for different probe polarizations (pump perpendicular to probe).

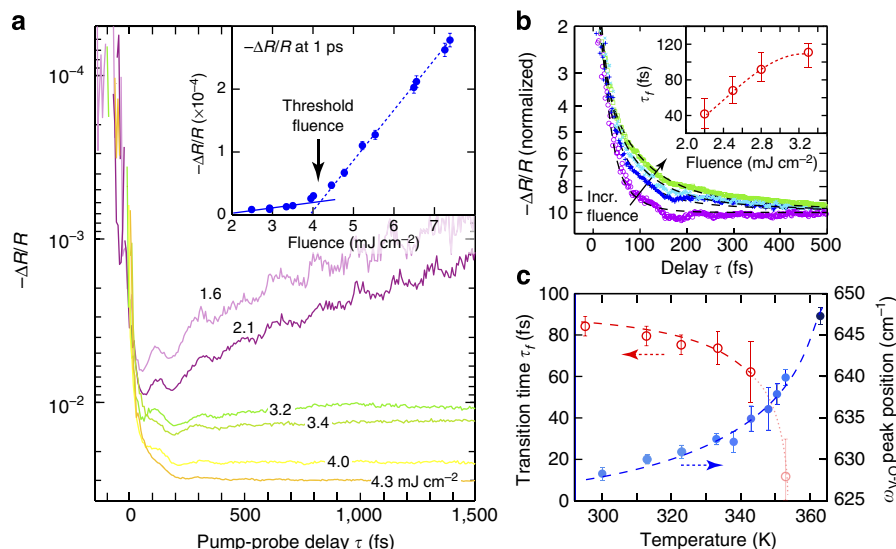


Figure 3 | Fluence and temperature dependence (a) Fluence-dependent transient reflectivity traces $-\Delta R/R$ for crystal #30. Inset shows the non-linear dependence of the reflectivity with fluence at $\tau = +1$ ps delay. (b) Change in short timescale dynamics with fluence for $F > F_{th}$, on crystal #13. Black lines show fits to exponential recovery behaviour, with extracted transition time τ_f shown in the inset. (c) Variation of transition time with temperature, measured at 3.3 mJ cm^{-2} , showing a decrease in τ_f with increasing temperature (crystal #30). This is correlated with a change in insulating structure, as monitored through the ω_{V-O} Raman mode (see Supplementary Table 2). Error bars are based on the uncertainties of the fit of equation (1) in τ_f , and a Lorentzian fit to the V-O phonon Raman line in ω_{V-O} . Blue and red dashed lines are guides to the eye.

for more details on the convolution procedure). $f(t)$ is modelled as a biexponential function:

$$f(t) = -\frac{R_\infty}{1+a} \left(e^{-t/\tau_f} + a e^{-t/\tau_s} \right) + R_\infty, \quad (1)$$

with τ_f the initial, ultrashort transition time, constrained to <1 ps. τ_s captures the longer timescale behaviour, with $2 \text{ ps} < \tau_s < 10 \text{ ps}$, R_∞ describes the magnitude of the reflectivity change and the parameter a sets the relative scaling of the fast and slow exponential terms. We find that the contribution from slow dynamics is generally small (that is, $a \ll 1$) and therefore we focus here on the short timescale dynamics captured by τ_f .

Representative fits of the transient reflectivity response for crystal #13 for a range of above-threshold fluences are shown in Fig. 3b (black dashed lines), with $-\Delta R/R$ normalized for clarity. For the <500 -fs range, the response is dominated by τ_f . We observe three distinct characteristics in the ultrafast initial response. First, for the lowest fluence investigated we see a transition time of $\tau_f = 40 \pm 8$ fs, shorter than the previously observed dynamics in any VO_2 sample, as discussed further below. Second, we observe a dramatic, up to threefold increase in transition time with increasing fluence (b, inset), in contrast to a decrease observed in previous work on polycrystalline films^{3,6}. Third, we see the transition time τ_f decrease with increasing sample temperature (Fig. 3c). During the measurement, we used sufficiently low laser repetition rates (<100 kHz) to allow complete relaxation to the initial insulating state, thus minimizing the effects due to hysteresis that can occur close to the transition temperature. Through the combination with Raman spectroscopy, we can correlate this temperature-dependent change with the structural changes of the insulating phase on heating, as has been observed previously²⁷. The pump-probe measurement at $T = 352$ K has a small change in transient reflectivity and large uncertainty, since at this temperature metallic domains have appeared due to thermal excitation.

The data shown in Fig. 3 are for two different microcrystals. Figure. 3a,c shows fluence and temperature dependence for

crystal #30 (see Supplementary Fig. 1 and Supplementary Note 1 for discussion of hysteresis effects during the thermal MIT transition) and Fig. 3b shows data for crystal #13, respectively. The trends of an increase in τ_f with increasing fluence and a decrease in τ_f with increasing temperature are seen for all measured microcrystals, though extracted transition times vary between crystals. The transition times τ_f obtained from all measurements on 28 microcrystals of different sizes, and for selected different initial temperatures, and range of fluences are summarized in Fig. 4 and Supplementary Table 1. The values are shown as a function of the measured ω_{V-O} phonon frequency from Raman spectroscopy, as a proxy for the different insulating phases of the crystals (indicated by green-blue colour bar for the M1, T and M2 phases). The error bars are based on the statistical uncertainties of the fit of equation (1) in τ_f , and a Lorentzian fit to the V-O phonon Raman line in ω_{V-O} . Different microcrystal widths are indicated by the size of the data symbols (see legend), from $<5 \mu\text{m}$ to $>15 \mu\text{m}$. The fluences used are all above the threshold fluence for the specific microcrystal, with values indicated using false colour. The values of τ_f vary reproducibly from 40 to 200 fs for each crystallite. Notably, the average value of τ_f over all microcrystals is found to be $\bar{\tau}_f = 80 \pm 25$ with $\bar{\tau}_f^{-1} = \sum_i \tau_{f,i}^{-1}$ (blue circle). This value is in striking agreement with transition times τ_{TF} from thin-film studies⁵ (Fig. 4b).

s-SNOM imaging. The large variations in τ_f indicate that the photoinduced IMT is highly sensitive with respect to unknown electronic or structural heterogeneities between different crystallites. This inhomogeneity appears to be uncorrelated with structure, strain, temperature or microcrystal size, with no consistent behaviour even between crystals attached to the substrate (that is, strained) or free. This suggests a high susceptibility of τ_f to minor variations in doping, stoichiometric details or defects. These variations are small enough that they are not reflected in the lattice structure at the level detectable by few-wavenumber Raman shifts, nor in the macroscopic strain or temperature

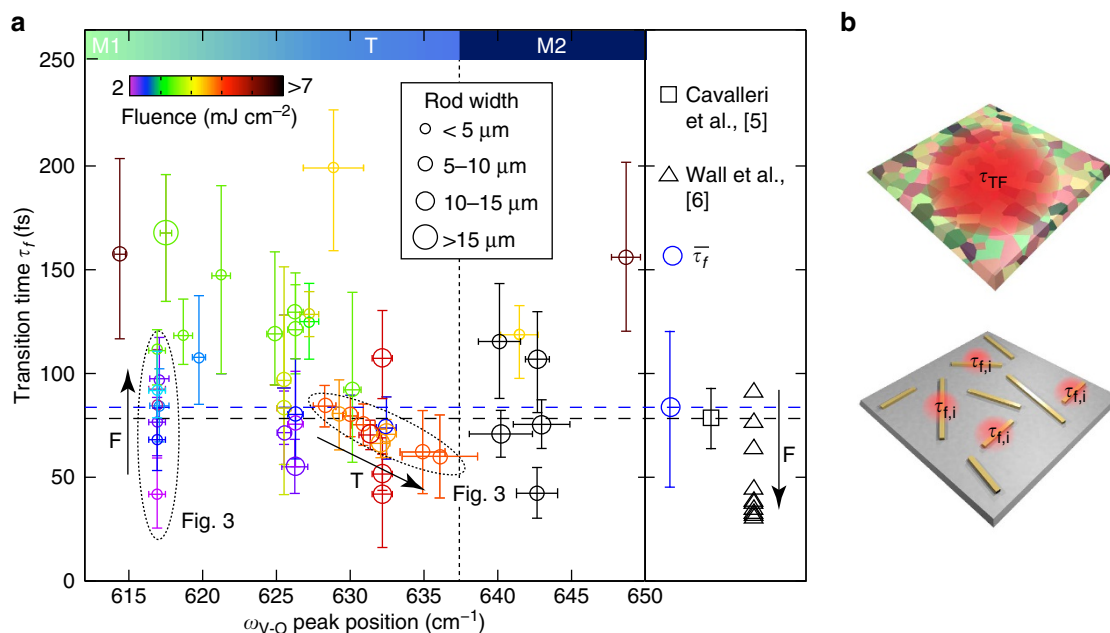


Figure 4 | Inhomogeneity of the ultrafast IMT (a) Photoinduced transition time τ_f , plotted against initial ambient insulating phase, represented by the frequency of the Raman mode ω_{V-O} . Error bars are based on the uncertainties of the fit of equation (1) in τ_f and a Lorentzian fit to the V-O phonon Raman line in ω_{V-O} . Colour bar at top shows corresponding insulating phases. Symbol size reflects microcrystal width, from $< 5 \mu\text{m}$, to $> 15 \mu\text{m}$. Symbol colour indicates pump fluence, from 2 mJ cm^{-2} (orange) to $> 7 \text{ mJ cm}^{-2}$ (black). τ_f varies from ~ 40 to ~ 200 fs, with no clear correlation with insulating phase. Dashed ovals indicate data sets shown in Fig. 3. Average transition time of all microrod measurements $\bar{\tau}_f = (80 \pm 25)$ fs (blue circle/line), compared with (75 ± 15) fs from Cavalleri *et al.*⁵ (black square/dashed line) observed in thin film samples. Time constants by Wall *et al.*⁶ from polycrystalline films (525 nm probe wavelength), where a decrease in time constant is observed with increasing fluence, in contrast the behaviour observed here for single crystals. (b) Schematic of thin film (top, τ_{TF}) versus single crystal (bottom, $\tau_{f,i}$) behaviour.

dependence of the IMT. They in turn may be spatially inhomogeneous and lead to spatial variations in the IMT on the intracrystalline level.

We take advantage of the complex phase behaviour of microcrystals attached to the substrate, where the minimization of strain to accommodate the different thermal expansions of VO_2 and the silicon substrate leads to the formation of metallic stripe domains along the c_R -axis²⁶ (Fig. 5). These mesoscopic domains with the spatial phase coexistence of metallic and insulating regions provides a sensitive measure to resolve the effect of microscopic inhomogeneities on the thermal IMT, from the interplay of extrinsic strain with localized defects and impurities.

Figure 5a shows a schematic of *s*-SNOM nano-infrared probing of the Drude dielectric response of VO_2 microcrystals on heating and cooling through the phase transition, with ~ 10 nm spatial resolution. Figure 5b shows the formation of mesoscopic metallic stripe domains perpendicular to the c_R -axis on cooling, with straight domain walls and homogeneous behaviour initially as the insulating states begin to form. Panels c and d then show the gradual narrowing of the metallic domains on further cooling, associated with the emergence of complex, meandering domain walls, with details very sensitive to temperature. The metallic domains then begin to break up in the direction perpendicular to the c_R -axis (Fig. 5e–g). The domain wall roughening and inhomogeneous disappearance of the metallic puddles on cooling is highly variable with repeated temperature cycling (see Supplementary Fig. 2).

This nanoscale thermal domain behaviour, with both reproducible and non-reproducible spatial features, together with the variability of the ultrafast IMT dynamics, supports a hypothesis of an electronically driven transition, yet sensitively affected by both

static and dynamic variations in the local properties, as discussed further below.

Discussion

In the following, we discuss the implications of the experimental observations of the ultrafast photoinduced IMT dynamics and thermal spatial nanodomain behaviour of single VO_2 microcrystals, especially with regard to the interpretation of previous experiments on polycrystalline thin films.

Below threshold, we resolve the dynamical response of the two low-frequency modes in the coherent phonon spectrum, at ~ 200 and $\sim 225 \text{ cm}^{-1}$. These modes are of A_{1g} symmetry, and are attributed to twisting of vanadium dimers, with their relative strength depending on the type of insulating phase and crystal orientation with respect to pump and probe polarization^{34,38}. Frequencies and linewidths are consistent with corresponding incoherent Raman scattering and track the different insulating phases, of M1, M2 and triclinic with their characteristic frequencies. Previous coherent phonon measurements have disagreed in whether one or two phonon modes are observed in the 200-cm^{-1} range (6 THz vicinity), and in their precise frequencies^{35,39}. These findings can now be reconciled given possible different insulating phases of the crystallites in the thin films. The modes that are observed can depend on both number and relative orientation of the ensemble of crystallites probed in polycrystalline films.

Above the fluence threshold for the IMT, we observe ultrafast dynamics on the tens of fs timescale, with a collapse in the bandgap of the insulating phase. In thin film measurements, the fluence-dependent behaviour has been divided into three regimes^{6,7}: below threshold, where coherent phonons are

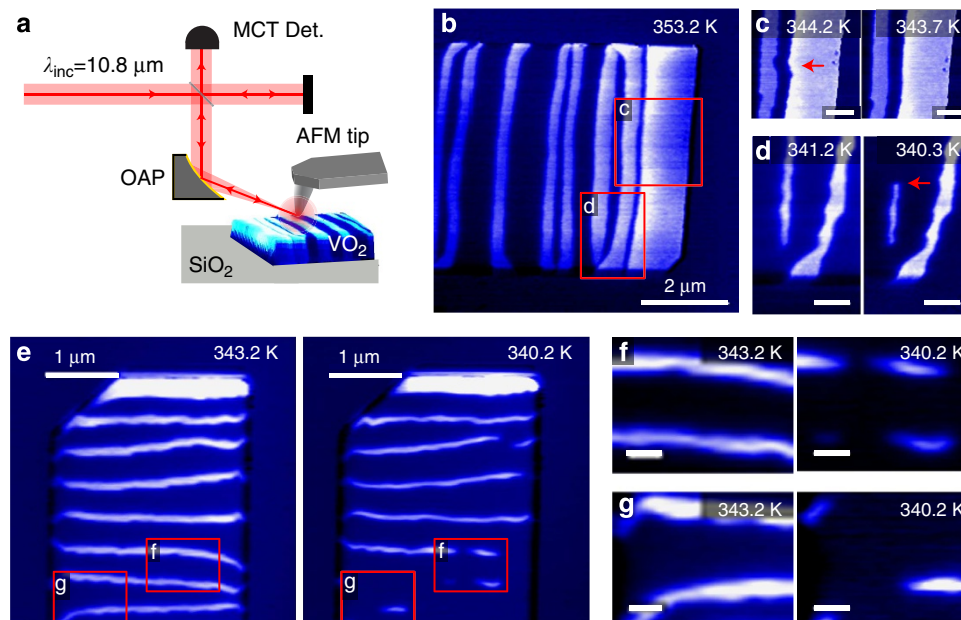


Figure 5 | Nanoscale inhomogeneity of thermal IMT (a) Schematic of Drude response *s*-SNOM. (b) When heating through the metal-insulator transition, the microcrystals form alternating metallic (bright) and insulating (dark) domains perpendicular with respect to the c_R -axis to minimize substrate strain²⁶. On cooling, the metallic domains gradually narrow and become irregular, eventually breaking into small metallic puddles, with texture sensitive to small variations in temperature (c,d,f,g show the evolution of corresponding fine structural details). Over repeated cooling cycles, the domains break in different locations and at varying temperatures (see Supplementary Fig. 2 and Supplementary Note 2). The scale bars in b,c and f,g are 500 and 200 nm, respectively.

resolved; above threshold, where the system is driven into the metallic state but thermal effects are visible over longer timescales; and a saturation regime, where the magnitude of the transient reflectivity signal saturates and long timescale thermal behaviour is no longer observed. In contrast, our fluence-dependent measurements on single microcrystals show only two distinct fluence regimes (Fig. 3): the below-threshold regime where coherent phonons are observed and the reflectivity relaxes on picosecond timescales, and the above-threshold regime with emergence of the metastable metallic phase and no long timescale (ps) thermal behaviour. In the saturation regime of thin films, in general, the rapid initial change and persistence of the change in reflectivity indicates that the entire probed volume experiences an ultrafast photoinduced transition to a metal-like state. Since the crystals are thinner than the penetration depth of ~ 180 nm at 800 nm wavelength, a homogeneous excitation of the microcrystal can be assumed for all above-threshold fluences with the increase in transient reflectivity with increasing fluence attributed to greater excitation density. This is supported by the observation that the microcrystal thickness does not appear to affect transition time. Hence, we conclude that the microcrystal fluence-dependent behaviour differs from the thin films due to its lack of inhomogeneous crystallite contributions, with different threshold fluences, which produce the effective intermediate 'above-threshold' regime in thin films.

Most notably, we find that the initial insulating phase (M1, M2 or T) has no influence on the dynamics of the ultrafast IMT. Furthermore, crystals with apparently identical lattice structure as concluded from identical Raman spectra reveal different photoinduced transition timescales. This suggests that the emergence of the metallic phase in the photoinduced IMT is not a lattice related effect and the variations in the IMT dynamics point to an electronic delocalization transition.

With the transition times observed below the 75-fs half-cycle period of the $\omega_{V1,V2}$ phonon modes, the fastest being 40 ± 8 fs,

across a range of fluences, we deduce that the 150-fs timescale for breaking the V–V dimer bonds does not pose a rate-limiting step for the formation of the metallic state of the photoinduced transition, as originally proposed by Cavalleri *et al.*^{5,15}. Our range of timescales is similar to that reported by Wall *et al.*⁶ shown in Fig. 4, but their results are not directly comparable since they are based on a model with additional time constants and fitting parameters, and were extracted from dynamics measured at a different probe wavelength. We also note that Wall *et al.*⁶ additionally observed a strong dependence of the dynamics on wavelength. While measurements close to the fluence threshold may contain fast contributions from photoexcited carriers without an associated bandgap collapse, all measurements shown in Fig. 4a show a persistent, long timescale reflectivity change up to microseconds in duration with no subsequent relaxation on the few-ps timescale, indicating an electronic phase change. We also note that very low fluence thresholds for the electronic transition and a monoclinic metallic phase have been proposed recently^{36,40}, which is consistent with our observations. Our results also suggest a finite response time for the transition⁴⁰.

The electronic origin of the dynamics is supported by the decrease in transition time observed on heating the microcrystals. While the free energy change with the increase in temperature is small⁴¹ compared with the energy deposited by the pump pulse, the change in dynamics we observe is substantial. The insulating phase also changes with increasing temperature, following the progression M1–T–M2 (as shown in Fig. 3), but the structural change in itself appears to have no effect on the transition time, as discussed above. This temperature-dependent decrease in transition time is an interesting counterpoint to the increase in transition time with increasing fluence. This behaviour is in contrast to Wall *et al.*, whose time constants all decreased with increasing fluence⁶. Our results support the hypothesis of a possible artifact of thin-film polycrystalline studies, which probe an ensemble averaged response of variable numbers of crystallites,

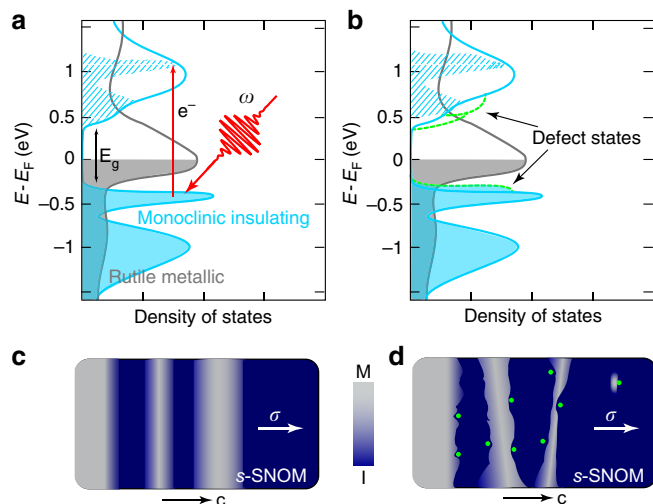


Figure 6 | Perturbation of the electronic structure and dynamics by defects or impurities (a) Schematic representation showing the electronic band structure of VO₂ and (b) possible modifications by defects or impurities (green dashed lines), which could modify the transition dynamics of the ultrafast IMT and produce the variable dynamics observed. These defects could also sensitively affect the spatial IMT nanodomain behaviour as observed experimentally (c,d).

each with varying transition times and threshold fluences. The ensemble measurement will therefore appear to be a superposition of multiple timescales, requiring a larger number of fitting parameters and producing different fluence-dependent behaviour.

Fluence behaviours similar to that observed here were previously observed in graphite⁴² and Cr-doped V₂O₃ (ref. 43). For VO₂, this could suggest that the higher fluences drive the system further out of equilibrium and lead to slower transition times to the metallic state. A possible mechanism would be non-equilibrium interband excitations, with variable fractional pump-induced occupation depending on the density of states and its variation with doping and impurities, to states supporting or opposing band structure collapse, as illustrated schematically in Fig. 6a,b. Saturation of states favourable to fast transitions could occur at higher fluences, and would lead to slower dynamics with increasing fluence due to increased excitation of states opposing band structure collapse. The increase in transition time with increasing fluence could also be indicative of a transition driven by an overdamped phonon response, where the damping increases with increasing fluences and leads to slower dynamics. The presence of defects and spatial variations in local doping or strain could furthermore pin domain walls and produce the meandering domain structure we resolve experimentally domain walls (Fig. 6c,d).

In summary, even on the individual-crystal level for nominally homogeneous single crystals, we observe a highly inhomogeneous IMT behaviour, with dynamics ranging from ~40 to ~200 fs. In addition, *s*-SNOM imaging of the thermal transition also shows inter- and intracrystal inhomogeneity, with variability of the metallic domains on cooling indicating that the VO₂ microcrystals are in a highly dynamic state close to the critical temperature *T_C*. We therefore conclude that in thin films the intrinsic dynamics can be masked by the inhomogeneous distribution and complicating extrinsic interactions among crystallites. Yet, even on the single-crystal level, both the ultrafast photoinduced studies and thermal IMT *s*-SNOM indicate a high degree of sensitivity to, for example, dopants and defects. These

could alter the density of available states and the redistribution of photoexcited holes and electrons, and thereby change the rate of electron delocalization and subsequent bandgap collapse. Similarly, defects and complex strain could disrupt the free energy uniformity and produce complex domain topology in the thermal transition. Further study of the broadband response of microcrystals could help to elucidate the nature and specific influence of these defects on the mechanism of the IMT. These results raise the question of how to access the intrinsic response of VO₂, and that of strongly correlated electron materials more generally. Our results call for more precise characterization of VO₂ and other samples, given that the rich and diverse properties of these materials that can be induced and controlled through, e.g., doping, strain, external fields may be more sensitive to disorder and impurities than previously expected.

Methods

Sample details and Raman characterization. The single-crystal vanadium dioxide microcrystals were grown by vapour phase transport on an oxidized silicon substrate²⁴. This produces rectangular cross-sectional microcrystals of varying sizes and orientations, as shown in Fig. 1d. Typically, the crystals have widths of 100 nm – 15 μm, and lengths up to 1 mm. The rutile *c*-axis (*c_R*) is along the length of the rod.

To characterize the individual microcrystals, a home-built Raman microscope with HeNe laser excitation ($\lambda = 632.8$ nm) and a 0.8 NA objective (Olympus) is used, with 2 cm⁻¹ spectral resolution. The three insulating structural phases, monoclinic M1, monoclinic M2 and triclinic T, are distinguished principally through the position of the 610–650 cm⁻¹ phonon mode, ω_{V-O} (Fig. 2a)²⁷. Microcrystals with ω_{V-O} close to 650 cm⁻¹ are in the M2 phase, which can be produced by substrate strain or ~2% Cr doping^{26,27}. For microcrystals in the M1 phase, $\omega_{V-O} \sim 620$ cm⁻¹, and the amount of doping or impurity is < 1% (ref. 44).

Ultrafast pump-probe microscopy. The photoinduced IMT in individual microcrystals is studied by degenerate pump and probe microscopy based on a regenerative amplified Ti:S system (Wyvern, KMLabs), which produces 45 fs pulses at 800 nm (Fig. 1b), with a variable repetition rate from 10 to 350 kHz. A 95:5% beamsplitter separates the incident light into the pump and probe arms. The two beams are then recombined with a small spatial offset, passed through a dual-frequency optical chopper, and focused onto the sample using an off-axis parabolic mirror with probe focus size ~15 μm and pump focus size ~30 μm. Variable pump fluences of up to 10s of mJ cm⁻² are used. The back-reflected probe, selected by polarization, is detected by a photodiode with lock-in amplification to improve the signal-to-noise ratio. The pump and probe polarizations are orthogonal. FROG is used to characterize the pump and probe pulse transient phase $\phi(t)$ and amplitude $A(t)$. With the intensity profile $I(t) = A(t)^2$, we convolute the fitting function in the frequency domain to obtain $-\Delta R/R(t) = I(t) \otimes f(t)$ where $f(t)$ is a biexponential function given in equation 1.

***s*-SNOM measurements.** The samples are mounted on a resistive heater with a thermocouple to enable temperature control within absolute uncertainty ± 0.5 K. Atomic force microscopy measurements are used to characterize the heights of the rods chosen for measurements. The rods have rectangular cross-sections with thicknesses of 25–200 nm (Fig. 1e). Simultaneous with the atomic force microscopy measurements, we perform *s*-SNOM with a $\lambda = 10.8$ μm CO₂ laser source to probe the changes in local reflectivity due to the IMT.

References

- Morin, F. J. Oxides which show a metal-to-insulator transition at the Neel temperature. *Phys. Rev. Lett.* **3**, 34–36 (1959).
- Imada, M., Fujimori, A. & Tokura, Y. Metal-insulator transitions. *Rev. Mod. Phys.* **70**, 1039–1263 (1998).
- Cavalleri, A. *et al.* Femtosecond structural dynamics in VO₂ during an ultrafast solid-solid phase transition. *Phys. Rev. Lett.* **87**, 237401 (2001).
- Becker, M. F. *et al.* Femtosecond laser excitation of the semiconductor-metal phase transition in VO₂. *Appl. Phys. Lett.* **65**, 1507–1509 (1994).
- Cavalleri, A., Dekorsy, T., Chong, H. H. W., Kieffer, J. C. & Schoenlein, R. W. Evidence for a structurally-driven insulator-to-metal transition in VO₂: a view from the ultrafast timescale. *Phys. Rev. B* **70**, 161102 (2004).
- Wall, S. *et al.* Tracking the evolution of electronic and structural properties of VO₂ during the ultrafast photoinduced insulator-metal transition. *Phys. Rev. B* **87**, 115126 (2013).
- Kübler, C. *et al.* Coherent structural dynamics and electronic correlations during an ultrafast insulator-to-metal phase transition in VO₂. *Phys. Rev. Lett.* **99**, 116401 (2007).

8. Nakajima, M., Takubo, N., Hiroi, Z., Ueda, Y. & Suemoto, T. Photoinduced metallic state in VO₂ probed by the terahertz pump-probe spectroscopy. *Appl. Phys. Lett.* **92**, 011907 (2008).
9. Xue, X. *et al.* Photoinduced insulator-metal phase transition and the metallic phase propagation in VO₂ films investigated by time-resolved terahertz spectroscopy. *J. Appl. Phys.* **114**, 193506 (2013).
10. Cavalleri, A. *et al.* Band-selective measurements of electron dynamics in VO₂ using femtosecond near-edge X-ray absorption. *Phys. Rev. Lett.* **95**, 067405 (2005).
11. Cavalleri, A. *et al.* Picosecond soft X-ray absorption measurement of the photoinduced insulator-to-metal transition in VO₂. *Phys. Rev. B* **69**, 153106 (2004).
12. Hada, M., Okimura, K. & Matsuo, J. Characterization of structural dynamics of VO₂ thin film on c-Al₂O₃ using in-air time-resolved X-ray diffraction. *Phys. Rev. B* **82**, 153401 (2010).
13. Grinfelds, M. S., Lobastov, V. A., Weissenrieder, J. & Zewail, A. H. Four-dimensional ultrafast electron microscopy of phase transitions. *Proc. Natl Acad. Sci. USA* **103**, 18427–18431 (2006).
14. Lobastov, V. A., Weissenrieder, J., Tang, J. & Zewail, A. H. Ultrafast electron microscopy (UEM): four-dimensional imaging and diffraction of nanostructures during phase transitions. *Nano Lett.* **7**, 2552–2558 (2007).
15. Baum, P., Yang, D.-S. & Zewail, A. H. 4d visualization of transitional structures in phase transformations by electron diffraction. *Science* **318**, 788–792 (2007).
16. Mott, N. F. Metal-insulator transition. *Rev. Mod. Phys.* **40**, 677–683 (1968).
17. Zylbersztein, A. & Mott, N. F. Metal-insulator transition in vanadium dioxide. *Phys. Rev. B* **11**, 4383–4395 (1975).
18. Qazilbash, M. M. *et al.* Mott transition in VO₂ revealed by infrared spectroscopy and nano-imaging. *Science* **318**, 1750–1753 (2007).
19. Tao, Z. *et al.* Decoupling of structural and electronic phase transitions in VO₂. *Phys. Rev. Lett.* **109**, 166406 (2012).
20. Warwick, M. E. A. & Binions, R. Advances in thermochromic vanadium dioxide films. *J. Mater. Chem. A* **2**, 3275–3292 (2014).
21. Lysenko, S., Fernandez, F., Rúa, A. & Liu, H. Ultrafast light scattering imaging of multi-scale transition dynamics in vanadium dioxide. *J. Appl. Phys.* **114**, 153514 (2013).
22. Liu, H., Kwon, O.-H., Tang, J. & Zewail, A. H. 4d imaging and diffraction dynamics of single-particle phase transition in heterogeneous ensembles. *Nano Lett.* **14**, 946–954 (2014).
23. Huffman, T. J. *et al.* Anisotropic infrared response of vanadium dioxide microcrystals. *Phys. Rev. B* **87**, 115121 (2013).
24. Guiton, B. S., Gu, Q., Prieto, A. L., Gudiksen, M. S. & Park, H. Single-crystalline vanadium dioxide nanowires with rectangular cross sections. *J. Am. Chem. Soc.* **127**, 498–499 (2005).
25. Wu, J. *et al.* Strain-induced self organization of metal-insulator domains in single-crystalline VO₂ nanobeams. *Nano Lett.* **6**, 2313–2317 (2006).
26. Jones, A. C., Berweger, S., Wei, J., Cobden, D. & Raschke, M. B. Nano-optical investigations of the metal-insulator phase behavior of individual VO₂ microcrystals. *Nano Lett.* **10**, 1574–1581 (2010).
27. Atkin, J. M. *et al.* Strain and temperature dependence of the insulating phases of VO₂ near the metal-insulator transition. *Phys. Rev. B* **85**, 020101 (2012).
28. Park, J. H. *et al.* Measurement of a solid-state triple point at the metal-insulator transition in VO₂. *Nature* **500**, 431–434 (2013).
29. Cao, J. *et al.* Strain engineering and one-dimensional organization of metal-insulator domains in single-crystal vanadium dioxide beams. *Nat. Nanotechnol.* **4**, 732–737 (2009).
30. Cao, J. *et al.* Extended mapping and exploration of the vanadium dioxide stress-temperature phase diagram. *Nano Lett.* **10**, 2667–2673 (2010).
31. Tselev, A. *et al.* Symmetry relationship and strain-induced transitions between insulating M1 and M2 and metallic R phases of vanadium dioxide. *Nano Lett.* **10**, 4409–4416 (2010).
32. Verleur, H. W., Barker, A. S. & Berglund, C. N. Optical properties of VO₂ between 0.25 and 5 eV. *Phys. Rev.* **172**, 788–798 (1968).
33. van Veenendaal, M. Ultrafast photoinduced insulator-to-metal transitions in vanadium dioxide. *Phys. Rev. B* **87**, 235118 (2013).
34. Zeiger, H. J. *et al.* Theory for dispersive excitation of coherent phonons. *Phys. Rev. B* **45**, 768–778 (1992).
35. Kim, H.-T. *et al.* Monoclinic and correlated metal phase in VO₂ as evidence of the Mott transition: coherent phonon analysis. *Phys. Rev. Lett.* **97**, 266401 (2006).
36. Morrison, V. R. *et al.* A photoinduced metal-like phase of monoclinic VO₂ revealed by ultrafast electron diffraction. *Science* **346**, 445–448 (2014).
37. Cocker, T. L. *et al.* Phase diagram of the ultrafast photoinduced insulator-metal transition in vanadium dioxide. *Phys. Rev. B* **85**, 155120 (2012).
38. Schilbe, P. Raman scattering in VO₂. *Physica B* **316**, 600–602 (2002).
39. Wall, S. *et al.* Ultrafast changes in lattice symmetry probed by coherent phonons. *Nat. Commun.* **3**, 721 (2012).
40. Wegkamp, D. *et al.* Instantaneous band gap collapse in photoexcited monoclinic VO₂ due to photocarrier doping. *Phys. Rev. Lett.* **113**, 216401 (2014).
41. Pouget, J. P. *et al.* Dimerization of a linear Heisenberg chain in the insulating phases of V_{1-x}Cr_xO₂. *Phys. Rev. B* **10**, 1801 (1974).
42. Ishioka, K. *et al.* Ultrafast electron-phonon decoupling in graphite. *Phys. Rev. B* **77**, 121402 (2008).
43. Mansart, B., Boschetto, D., Sauvage, S., Rousse, A. & Marsi, M. Mott transition in Cr-doped V₂O₃ studied by ultrafast reflectivity: electron correlation effects on the transient response. *Europhys. Lett.* **92**, 37007 (2010).
44. Marini, C. *et al.* Optical properties of V_{1-x}Cr_xO₂ compounds under high pressure. *Phys. Rev. B* **77**, 235111 (2008).

Acknowledgements

We thank Eric Muller for help with data fitting and the deconvolution procedure. Funding was provided from the U.S. Department of Energy, Office of Basic Sciences, Division of Materials Sciences and Engineering, under Award No. DE-FG02-12ER46893 (Raschke) and BES IDE-SC0002197 (Cobden).

Author contributions

A.C.J. designed the experiment. B.T.O. and A.C.J. performed the measurements, with J.H.P. and D.H.C. providing the samples. J.M.A. and B.T.O. analysed the data, and J.M.A. contributed to the interpretation of results. M.B.R. and D.H.C. conceived the experiments and contributed to the interpretation of results.

Additional information

Supplementary Information accompanies this paper at <http://www.nature.com/naturecommunications>

Competing financial interests: The authors declare no competing financial interests.

Reprints and permission information is available online at <http://npj.nature.com/reprintsandpermissions/>

How to cite this article: O'Callahan, B. T. *et al.* Inhomogeneity of the ultrafast insulator-to-metal transition dynamics of VO₂. *Nat. Commun.* **6**:6849 doi: 10.1038/ncomms7849 (2015).